# 1
# Bulk growth of SiC – review on advances of SiC vapor growth for improved doping and systematic study on dislocation evolution

*Sakwe Aloysius Sakwe, Mathias Stockmeier, Philip Hens, Ralf Müller, Desirée Queren, Ulrike Kunecke, Katja Konias, Rainer Hock, Andreas Magerl, Michel Pons, Albrecht Winnacker, and Peter Wellmann*

## 1.1 Introduction

State of the art bulk growth of SiC crystals is carried out by the seeded sublimation, often referred to as physical vapor transport (PVT) growth method. Today, 3 inch and 4 inch 4H-SiC wafers are commercially available with almost zero micropipe density and dislocation densities in the low $10^4$ $cm^{-2}$ range. The present contribution summarizes research that has been performed by the authors in recent years using advanced growth techniques for improved doping, for control of gas phase composition, and for a deeper understanding of defect formation, i.e. dislocation dynamics, during SiC bulk crystal growth. Much of the work was carried out using a modified physical vapor transport (M-PVT) setup that uses an extra gas pipe for feeding of a small amount of additional gases into the growth cell [1–5]. With this technique, for the first time, p-type aluminum doping of SiC was realized with resistivities of as low as 0.1 Ω cm . . . 0.2 Ω cm that meet electronic device requirements [6]. In addition, the highest in-situ n-type phosphorus doping using phosphine with chemical concentrations above $10^{18}$ $cm^{-3}$ could be realized [7]. For the quantitative electrical characterization optical techniques, such as optical absorption and Raman spectroscopy, were applied in addition to or as replacement for purely electrical measurements [8–18]. Numerical modeling was successfully applied to understand mass transfer and growth in the M-PVT growth configuration [4, 5, 19–21]. Mass transport investigations were also conducted in the conventional PVT configuration using the carbon isotope $^{13}C$ [22–24]. The occurrence and vanishing of certain dislocation types with varying doping type, i.e. n-type and p-type doping were discovered. As a main result it was found that basal plane dislocations (BPDs) appear less pronounced or are even absent in p-type doped SiC, irrespective of dopant type, aluminum or boron acceptors, respectively [25–27]. This indicates that this dislocation type can be suppressed by p-type doping. The suppression of BPD generation in SiC by p-type doping could

*Silicon Carbide, Vol. 1: Growth, Defects, and Novel Applications*
Edited by Peter Friedrichs, Tsunenobu Kimoto, Lothar Ley, and Gerhard Pensl

ISBN: 978-3-527-40953-2

have a tremendous impact on high power electronic devices made from this material. This is because the generation and expansion of stacking faults due to the movement of BPDs will be suppressed as well. Recently, dislocation and defect generation studies were expanded to in-situ X-ray diffraction studies [28].

The following discussion focuses on new results in the field of dislocation dynamics. Besides doping, additional parameters such as growth temperature were taken into account. For the latter, a number of experiments were conducted in the conventional PVT growth configuration. Dislocation evolution was studied by a statistical approach, which will be explained in a forthcoming section.

## 1.2 Experiments

### 1.2.1 Crystal growth

Crystal growth was carried out using the PVT [29] and M-PVT methods [1–5, 30]. We performed several growth runs; the input parameters of interest during growth (growth temperature and doping) were altered in each run in such a way as to precisely compare dislocation evolution and dynamics with respect to them. Several crystals were grown at different temperatures in a series of growth runs, keeping all other conditions constant. In another series of growth runs the doping was varied; purely n-type doped (6H-SiC:N) and purely p-type doped (6H-SiC:Al or B) crystals were grown. The doping concentration for both doping types was in the low $10^{18}$ $cm^{-3}$ range.

For a reliable evaluation of the influence of these parameters on dislocation evolution it is important that all other growth conditions, which might influence dislocation formation, are kept constant in all growth runs; changes occurring due to run-to-run variations, such as temperature gradient, bending of lattice planes, etc., have to be kept minimal. This is, however, difficult to achieve practically and the best way to solve this problem is to design growth concepts that entail changing the parameters in a single crystal growth run, such that only those parameters under investigation are varied. As a result, different portions of the crystal are produced under different values of these parameters and the evolution of dislocations and their dynamic properties with respect to these can be traced out more accurately along the crystal growth axis.

To investigate, systematically, the influence of doping on dislocation evolution and dynamics sequential p-type and n-type doping during single crystal growth runs was implemented to produce p-type and n-type doped regions in the crystals, in addition to the purely p-type and n-type doped crystals described above. Three differently doped regions, i.e. p-type/n-type/p-type were produced sequentially in 6H-SiC single crystals. Crystal growth was carried out with constant p-type doping (Al or B acceptors) throughout the experiment time. After a period, $t_1$, of growth nitrogen gas in high concentration was intro-

duced into the growth chamber to overcompensate the p-type doping and to turn the crystal into n-type. After another period, $t_2$, the nitrogen co-doping was switched off, returning the crystal to p-type. The second p-type doping lasted for a period, $t_3$. Growth of the sequentially p-type/n-type/p-type doped crystals with boron as acceptor atoms for the p-type doping was carried out using the conventional PVT setup (the boron was mixed directly into the source material), while that of the sequentially p-type/n-type/p-type doped ones using aluminum as acceptors was performed using the M-PVT setup. For the sequential doping using boron as acceptors $t_1 = 20$ h, $t_2 = 25$ h and $t_3 = 20$ h, while in the case of aluminum as acceptor atoms $t_1 = t_2 = t_3 = 10$ h. In both cases growth was carried on the $(000\bar{1})$C plane.

The grown crystals were about 20 mm in thickness and the single crystal areas had diameters of about 40 mm. A typical longitudinal cut of the crystals (parallel to the *a*-plane) is shown in Fig. 1.1 to depict the p-type/n-type/p-type doped regions. The p-type doped regions are thicker than the n-type doped one because nitrogen doping reduces the growth rate as compared to doping with Al or B. In the n-type doped crystal region the net donor concentration is $N_D - N_A \approx 10^{19}$ cm$^{-3}$.

Both low and high doped n- and p-type crystals were evaluated regarding basal plane dislocations. The doping concentration in both doping types was in the range $n, p = 10^{16} - 10^{19}$ cm$^{-3}$ for the purely n- and p-type doped crystals and about $10^{17} - 10^{18}$ cm$^{-3}$ (p- and n-type doped regions) for the sequentially p-type/n-type/p-type doped ones as determined by optical absorption [31] and Hall measurements [32]. The seed crystals used in the growths were n-type doped ($n \approx 2 \times 10^{17}$ cm$^{-3}$). The crystals developed large facets of about 12–20 mm in diameter, thereby providing large areas for dislocation investigation not influenced by the polycrystalline rim.

To study the influence of the seed temperature (or growth interface temperature) on dislocation evolution and dynamics during growth we conducted a series of experiments with different input growth temperatures. During these experiments different approaches were applied to vary the temperature. Three sets of experiments were conducted:

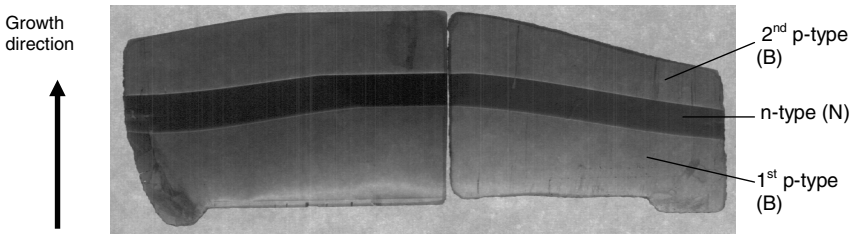


**Figure 1.1** Longitudinal cut through the sequentially p-type/n-type/p-type doped 6H-SiC showing the three doped regions. The dark region in the middle is the n-type doped region. The crack in the middle of the crystal occurred during machining of the sample.

(a) First, different crystal growth runs were carried out at different process temperatures. For each run standard growth conditions were implemented, i.e. constant growth temperature and pressure. However, the growth temperatures were varied between the runs. These growth experiments served as references to those with continuous temperature change described in points (b) and (c) below.

(b) Crystal growth was carried out in such a way that the growth temperature was increased continuously from about 2150 °C at the commencement of growth until about 2350 °C at the end of growth during a single growth run, while all other conditions remained constant.

(c) In the third set of experiments, a reverse temperature mode to that in (b) was implemented to serve as verification to the latter during dislocation analysis. The growth temperature was decreased continuously from about 2350 °C to about 1900 °C over the entire growth period.

During high-temperature growth we observed no graphitization of the source material and of the grown crystal. From our experience, graphitization of the crystal is common only if the source material is depleted to a great extent. We controlled and avoided this by monitoring the growth cell using an *in-situ* digital X-ray imaging technique [33].

For the crystals grown with continuous temperature change different portions of the crystals were grown at different temperatures. The temperature profiles for the applied growth temperature modes listed above (a–c) are shown in Fig. 1.2. In the three growth runs, growth was performed on nominally undoped n-type seeds ($n \approx 10^{17}$ cm$^{-3}$) on the (0001)Si surfaces in Ar atmosphere. The doping concentration in the crystals was in the low $10^{17}$ cm$^{-3}$ range. The graphite components used in the setups had similar ages with respect to usage and, hence, similar thermal properties. As such, differences in temperature gradients (e.g. radial temperature gradient) that would probably occur as a result of age-induced variations in, e.g., thermal conductivity could be ruled out.

For a continuous change of the process temperature during crystal growth, it is important that during dislocation analysis of wafers from such crystals, the temperature at which the wafer or the characterized wafer surface was pro-

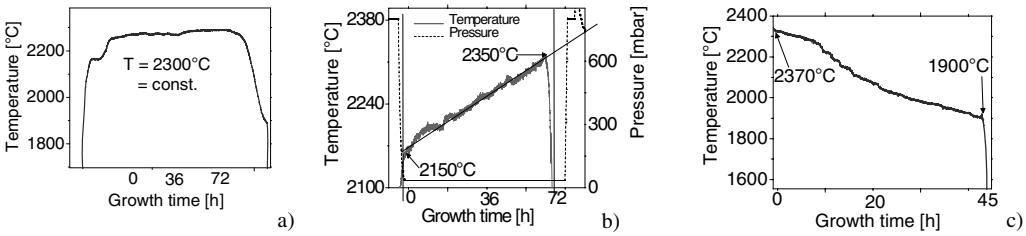


**Figure 1.2** Typical temperature profiles during growth of 6H-SiC crystals with constant temperature (a), continuous temperature increase (b), and continuous temperature decrease (c).

duced is known, in order to correlate the dislocation density to the temperature of crystal growth. Therefore, the digital *in-situ* X-ray imaging of the growth cell during the growth process was carried out at intervals of about 5 hours during the crystal growth period. The temperature and time at which this was done was recorded. Thus, the growth surface of each imaging step, for every increase in crystal thickness could be assigned to a particular growth temperature and time. Through these measurements, wafer surfaces in which dislocations were investigated could be assigned, with high accuracy, to particular growth temperatures and times. Material losses during the wafering steps were taken into consideration.

We performed crystallographic orientation of the as-grown crystals using Laue measurements in back reflection. A long flat was made perpendicular to the $[11\bar{2}0]$ direction, and a short one on the $[1\bar{1}00]$ direction. The flats not only facilitated dislocation tracking in the same crystal position, while characterizing the wafers but, also, characteristic spatial distributions of the dislocations could be related to certain crystallographic directions.

### 1.2.2 Characterization

To delineate the dislocations in the wafers we performed defect selective etching in molten KOH in a specially designed and calibrated etching furnace with *in-situ* temperature measurement configuration; the temperature measurements were carried out directly in the KOH melt. Details about the KOH defect etching furnace and optimization of the etching process for dislocation analysis are given elsewhere [34].

In order to further elaborate the structural properties of the materials with respect to the applied parameters of crystal growth we performed high energy X-ray diffraction (HE-XRD) measurements in a triple-axis configuration. The energy of the X-rays was 62.5 keV and penetration depths of up to 6 cm could be achieved, enabling imaging bulk SiC crystals for defects, e.g., sub-grain boundaries (SGB) or mosaic structures and, in addition, the bending of lattice planes. Detailed description of the HE-XRD triple-axis setup is given in Ref. [35].

Atomic force microscopy (AFM) measurements on the as-grown growth interfaces were carried out to study the step structure of the latter. From the step structure, in relation to crystal growth temperature, we could obtain information about kinetic processes at the growth front and their relation to dislocation evolution.

### 1.2.3 Evaluation of dislocation evolution and dynamics by statistical approach

This method involves dislocation analysis by dislocation tracking along the crystal growth axis, dislocation counting, and evaluation of their density in optimally etched wafers [34] of an oriented SiC crystal using optical microscopy

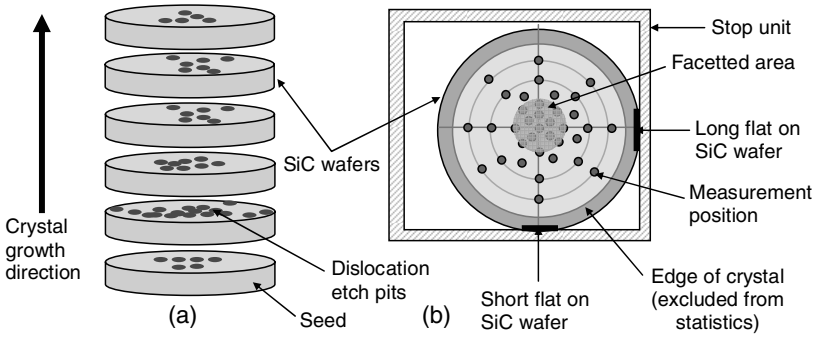


**Figure 1.3** Schematic presentation of the statistical approach method for the study of dislocation evolution and dynamics in SiC single crystal: (a) wafered crystal illustrating the scheme of etch pit tracking method, (b) illustration of the measured positions in the crystal and the positioning of the wafer on the optical microscope stage. Note that the flats are on the same position in all wafers, allowing measuring on the same crystal position.

for the etch pit visualization. Since each wafer represents a particular position in the crystal, it is possible to track the dislocations from wafer to wafer, i.e. along the length of the crystal on the same position. Figure 1.3 elucidates this principle (Fig. 1.3a: scheme of etch pit tracking and Fig. 1.3b: measured positions and wafer positioning on the microscope stage). The flats on the wafers and the stop unit on the microscope stage (Fig. 1.3b) enabled measurements on the same wafer positions. Analysis of the dislocation content and density at the same wafer positions provides information about their evolution and dynamics for the applied conditions of crystal growth. It is important to point out that in the dislocation tracking along the crystal growth axis we tracked but the dislocation density rather than a single defect. The data from dislocation statistics was used to interpret dislocation evolution. As a precaution, the edge of the crystal was excluded from the measurements and statistics in general to avoid dislocations that originate from extraneous effects that are not related to the growth parameters, such as spontaneous nucleation at the graphite wall surrounding the crystal during growth. Measurements were, therefore, concentrated in the facetted area and areas immediately outside the facet of the crystals.

The density of each dislocation type was evaluated separately according to the criteria to assign the etch pits (formed by defect selective etching) to the dislocation type they represent. Previous studies have categorized the hexagonal etch pits revealed on the vicinal (0001)Si face into three sizes: large, medium and small ones [36, 37] corresponding to micropipes (MPs), threading screw dislocations (TSDs), and threading edge dislocations (TEDs) respectively. Normally, the size of the etch pit is proportional to the strain energy (strain field) of the dislocation, which in turn, is proportional to the value of the Burgers vector. During defect selective etching at optimal etching condi-

tions, the strained areas are preferentially etched to produce the etch pits. Their sizes will, therefore, be proportional to the sizes of the strain fields. As such, a MP-related etch pit should be larger than that of a TSD, which, in turn, should be larger than that of a TED since the trend in their Burgers vectors is also MP > TSD > TED. BPDs are recognized by their asymmetrical or oval shapes on the vicinal surface. Through this principle, we were able to analyze, distinctly, the various dislocation types in SiC.

## 1.3 Results and discussions

### 1.3.1 Influence of doping on basal plane dislocation evolution and dynamics in 6H-SiC

We have observed by optical microscopy of etched n-type and p-type doped wafers of 6H-SiC single crystals ($n$, $p \approx 10^{16}-10^{19}$ cm$^{-3}$) that basal plane dislocations (BPDs) are absent or at least appear in a very low density in p-type doped crystals compared to n-type doped ones. This observation was first made in purely n-type (N donors) and p-type (Al acceptors) doped crystals. In particular, on investigating a number of p-type doped wafers with doping concentrations in the mentioned range we observed no etch pits associated with BPDs. In the n-type doped counterparts, on the other hand, a large proportion of the etch pits were asymmetrical in shape and exhibited a pronounced basal plane component, even at low concentrations ($n \approx 10^{17}$ cm$^{-3}$). The results suggest a difference in BPD dynamics in p-type versus n-type doped SiC crystals. Doping determines, to a great extent, the stability of BPDs in n-type compared to p-type doped material and, also, the way in which stress relaxation takes place in them, i.e. the kind of dislocations formed during relaxation.

To further elaborate dislocation evolution and dynamics in SiC, and, in particular, the preferential occurrence of BPD in n-type doped as compared to p-type doped 6H-SiC in a systematic way we performed dislocation analysis in the sequentially p-type/n-type/p-type doped crystals. These will sometimes be designated henceforth as p–n–p doped crystals. They were, as compared to the purely p-type and n-type doped ones that were grown in seperate growth runs, produced under exactly the same conditions; the difference in the crystals was only in the doping. In Fig. 1.4 etching images taken from the facet area of wafers of n-type doped versus p-type doped regions of the 6H-SiC crystals (a) with boron as acceptors and (b) with aluminum as acceptors for the p-type doping are presented. In Fig. 1.5 the relative BPD density to the total dislocation density in the wafers from the p–n–p doped crystal regions has been plotted to show the variation in BPD density in the n-type versus p-type doped regions of the crystals (Fig. 1.5a: boron as acceptors and 1.5b: aluminum as acceptors).

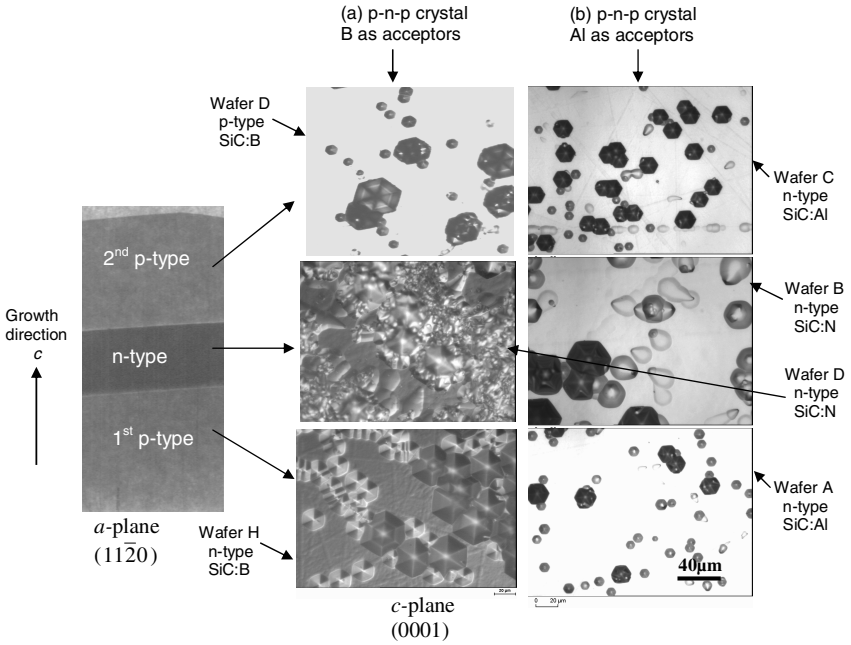


**Figure 1.4** Typical KOH etching images of sequentially p-type/n-type/p-type doped 6H-SiC crystals (see longitudinal cross section on the left of the figure) with Al and B as acceptors for the p-type doping (indicated) showing the variation of basal plane dislocation occurrence in the p-type and n-type doped sections of the crystals. Note the high basal plane dislocation density in the n-type doped region compared to the p-type doped one.

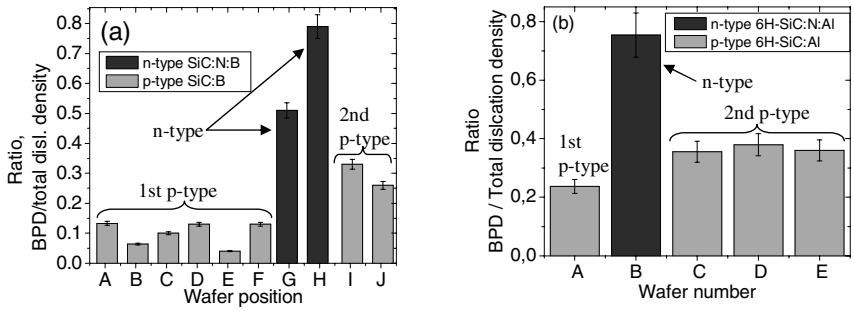


**Figure 1.5** Summary of dislocation statistics in the p-type/ n-type/p-type doped crystals showing the relative contribution of the basal plane dislocation density to the total dislocation density in the p-type and n-type regions.

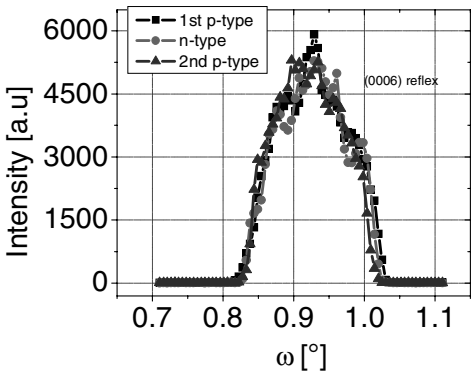


**Figure 1.6** Superimposed (0006) $\omega$ rocking curves of the p-type and n-type regions of the p–n–p doped 6H-SiC crystal. Note that the FWHM is the same in all the regions.

The BPD density is very low in the first p-type doped regions; increases dramatically in the n-type doped crystal parts, and decreases sharply again in the second p-type doped regions. The ratio of the BPD density to the overall dislocation density, which is the sum of BPDs, TEDs and TSDs is highest in the n-type doped regions of the crystals. TEDs dominate the overall dislocation density in the p-type doped regions. In the p−n−p doped crystals with boron as acceptors for the p-type doping the ratio is less than 0.2 in the first p-type doped region, rises acutely to about 0.9 in the n-type doped region and then falls drastically again to about 0.3 in the second p-type doped region. In the case of aluminum atoms as acceptors it is less than 0.3 in the first p-type doped region, rises dramatically to about 0.8 in the n-type region, and then falls to about 0.4 in the second p-type doped region. The overall dislocation density remained the same in the three differently doped regions.

Rocking curves in the three differently doped regions in the crystal with boron as acceptors are shown in Fig. 1.6 for the (0006) reflection, measured by means of high energy X-ray diffraction (HE-XRD) in a triple axis configuration [34]. The full width at half maximum (FWHM) is the same in the p-type/n-type/p-type doped regions (FWHM = 0.15°). It correlates with the tilt or twist in the crystals as a result of mosaicity and sub grain boundaries, which are closely related to the dislocation density, i.e. the greater the tilt (or the higher the dislocation density) the larger the FWHM. Chierchia et al. have suggested a way to estimate the dislocation density from the FWHM from the relationship (*tilt*) ~ (*dislocation density*)$^2$ [38]. In the above measurements the spot size of the X-ray beam was about 9 mm$^2$. The equality in the FWHM in the three differently doped regions is further evidence that the overall dislocation density in these regions is the same, but only the dominating dislocation types varies as determined by dislocation etch pit analysis after defect selective etching.

In the dislocation analysis in the differently doped crystal regions (Fig. 1.5) it can be noted that the BPD density in the p-type doped regions is not equal to zero as it is usually observed in purely p-type doped crystals. This is mainly due to the curved growth interface of the crystals (see Fig. 1.1). During cutting, some p-type and n-type wafers acquired sections of the opposite doping type in form of a ring. BPDs from the n-type inclusions could well affect dislocation statistics in the p-type regions. Also, the p-type wafers at the interfaces between the p-type and n-type doped regions, likewise that between the n-type seed and the first p-type region, could exhibit considerable BPDs especially if, due to wafering difficulties, a thin n-type layer is present in the p-type wafer. However, taking only a few points in the facet center of these crystals for dislocation analysis, the trend observed was high BPD density in n-type doped regions and almost no BPDs in the p-type doped regions.

No switch in polytype was induced across the transition areas between the p-type/n-type/p-type doped regions as measured by Raman spectroscopy. The Raman peaks in the differently doped regions, as well as in the transition regions were identical and corresponded to the polytype 6H (peaks not shown). Furthermore, HE-XRD measurements showed no change in lattice spacing ($d$-value) in the differently doped regions (Fig. 1.7). In the $2\theta$–$\omega$ scans in Fig. 1.7, the peak positions lie at the same $2\theta$ value for both the (0006) and ($\bar{2}$110) reflections (Fig. 1.7a and b). This might be due to the presence of acceptor atoms in both the p-type and n-type doped crystal regions. The influence of the acceptor atoms on lattice parameter seems to be greater than that of donor N atoms. Because of its small size, the N atom fits better in its C-lattice site than the acceptor atoms do in their Si-site. In the (0006) reflection the $d$-value in all the three regions is 2.53 Å and in the ($\bar{2}$110) reflection it is 1.56 Å. The lattice parameter continuity along the growth axis of the crystal in the three differently doped regions, as shown by the $2\theta$–$\omega$ scans (Fig. 1.7), rules out any lattice misfit at the interfaces between the differently doped re-

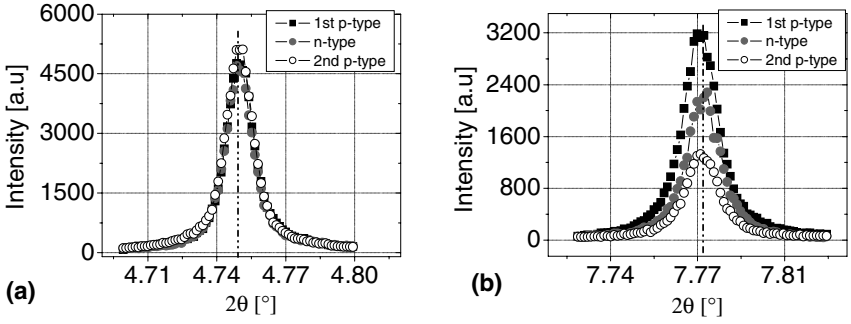


**Figure 1.7** Superimposed (0006) (a) and ($\bar{2}$110) (b) $2\theta$–$\omega$ scans of the p-type and n-type regions of the p–n–p doped 6H-SiC crystal (using boron for the p-type doping). The maximum peak intensities are on the same value of the Bragg angle ($2\theta$).

gions. Thus, the possibility of the formation of extra misfit dislocations in one region and not in the others can be ruled out. Lattice misfit is known to be associated with the formation of misfit dislocations, e.g., during heteroepitaxy, where the substrate and the epitaxial layer exhibit different lattice parameters [39].

#### 1.3.1.1 Basal plane dislocation dynamics in p-type versus n-type doped 6H-SiC

From the results of dislocation analysis in the p-type/n-type/p-type doped 6H-SiC crystals and, also, in the purely p-type and n-type doped ones it is admissible that doping may impact dislocation evolution and dynamics in different ways. Thermo-elastic strain relaxation in the p-type material seems to take place favoring entirely the generation of threading edge and screw dislocations, whereas in n-type doped material, on the other hand, this seems to take place favoring mostly the generation of basal plane dislocations (BPD).

In the discussion of the observed BPD phenomenon in n-type versus p-type doped 6H-SiC we consider the mechanical effects of the doping atoms in the crystal lattice (lattice hardness model) and, also, their electronic effects and the related Fermi energies (Fermi energy model) in the crystal.

##### 1.3.1.1.1 Doping-induced lattice hardness – lattice hardness model

It is generally observed in many crystal systems, that the addition of impurities into the crystal lattice induces strain in the crystal and, hence, changes its mechanical properties [40]. This is very common in metals and in semiconductors. In metallurgy the addition of impurities has been used as a means to impede dislocation movement, thereby hardening the material (impurity hardening [40]). Also, in single crystalline compound materials, e.g., compound semiconductors, impurities are known to affect the movement of dislocations. From the compound semiconductor material GaAs it is well known that doping with specific elements affects gliding along various slip planes in different ways; for instance, doping may lower glide in the closest packed (111) plane but favor it in others [41].

Also, in SiC, with six principal glide systems [42], doping may change the glide plane preference of dislocations. Most often, the basal plane slip is preferred for stress relaxation because less energy is required for glide [42]. The situation may change, or the glide system may be modified in different ways if the material is doped with either boron or aluminum acceptors or nitrogen donors because these atoms may exhibit different mechanical properties in the crystal lattice. Electro paramagnetic resonance (EPR) spectroscopy and electron nuclear double resonance (ENDOR) spectroscopy indicate that the acceptors Al and B occupy the Si-site [43] while N occupies the C-site [44] in SiC crystals. Because of differences in atomic radii $\Delta r$ between the substituting and substituted atoms ($\Delta r$ = 15 pm for Al, 25 pm for B, and 11 pm for N) and, also, the position of these atoms in the crystal lattice the stress exerted on the Si-site by the acceptor atoms B or Al should be different from that exerted by nitro-

**Table 1.1** Critical shear stress in n-type and p-type doped 6H-SiC [45].

| crystallographic direction of indentation | doping type | critical shear stress (GPa) |
|---|---|---|
| *c*-axis | n (SiC : N) | 7.30 ± 0.12 |
| *c*-axis | p (SiC : Al) | 7.94 ± 0.11 |
| *a*-axis | n (SiC : N) | 4.16 ± 0.11 |
| *a*-axis | p (SiC : Al) | 4.91 ± 0.06 |

gen on the C-site. Both the large compressive stresses as a result of the large Al atoms as well as the large tensile stresses exerted by the small boron atoms on the Si-site may impede the basal plane glide more efficiently than N atoms, which fit better in the C-sites. Thus, formation and glide of BPD would be hindered more in p-type doped than n-type doped SiC. Other glide systems, e.g., the prismatic slip, may become more favorable for stress relaxation than the basal plane slip.

This remark is supported by the results of critical shear stress measurements on n-type and p-type doped 6H-SiC samples in the *c*- and *a*-planes using nano-indentation [45]. The samples had doping concentrations ranging from $10^{18}$ cm$^{-3}$ – $10^{19}$ cm$^{-3}$. The results are summarized in Table 1.1. The p-type material exhibits a higher critical shear stress (CSS) along all investigated crystallographic directions as compared to the n-type doped one. In the *a*-axis (or [11$\bar{2}$0] direction), in particular, the critical shear stress is clearly by about 0.75 GPa, higher in the p-type doped 6H-SiC than in the n-type doped one. The CSS results indicate that n-type doped 6H-SiC is more vulnerable to basal plane dislocation formation than p-type 6H-SiC, signifying that in n-type doped 6H-SiC the formation of the latter dislocation type and their velocity would be higher than in the p-type doped counterpart.

#### 1.3.1.1.2 Fermi level model for basal plane dislocations

The lattice hardness model is not sufficient to explain the high BPD density in the n-type doped crystals as compared to the p-type doped ones in general. This is because in the study of the sequentially p-type/n-type/p-type doped crystals in which the n-type doped regions contain acceptors as well, and in the same concentration as in the p-type doped regions, the BPD density is still higher in the n-type doped regions than in the p-type doped ones. We realized n-type doping by overcompensation of the acceptors with excess nitrogen gas. If lattice hardening is the predominant effect, the p–n–p doped crystals could not have shown the variation in BPD density as found between the different p-type and n-type crystal regions. Hence, it is believed that the lattice hardness model alone does not explain the differences in the dislocation content of p-type doped versus n-type doped 6H-SiC crystals. Therefore, we suggest electronic effects, namely the differences in Fermi level positions due to doping as a possible model to explain, why basal plane dislocations are more stable in n-type than in p-type doped 6H-SiC.

It is well known in semiconductor technology that defects induce electronic levels in the band gap of the semiconductor [46]. Iwata et al. [47] have suggested that a stacking fault (SF) level at 0.6 eV below the conduction band minimum of n-type doped 4H-SiC may act as a quantum well, where electrons are trapped, thereby reducing the total energy of the system and, also, stabilizing the SF. This suggestion has been supported by theoretical studies of the electronic structure of such SFs in n-type 4H-SiC [47], and it is the authors' opinion that this may also apply to 6H-SiC.

In order for an electronically driven suppression of BPD generation for thermal stress relaxation to be valid, an electronic level of a BPD-induced defect would need to be present in the SiC crystal and its value would need to lie below the Fermi energy in n-type SiC and above the Fermi energy in p-type SiC. It could be argued that if the BPD would be occupied by an electron, it would be more stable than in an unoccupied state. Blumenau et al. suggested the presence of BPD-related energy levels at the bottom of the band gap [48]. In n-type SiC, with the Fermi level close to the conduction band, a BPD below this level would benefit from electron-capture and would be more stable than in p-type SiC with the Fermi level close to the valence band, and the BPD level being above it.

If the stability or dynamics of BPDs is dependent on the Fermi level, then it is important to estimate this at growth temperatures above 2000 °C since Fermi level and band gap depend on temperature (band gap shrinkage) [49]. We analyzed the Fermi levels ($E_F$) over a wide range of temperatures and, in particular, at typical growth temperatures and doping concentrations (see Fig. 1.8). For low doped n-type and p-type SiC ($n$, $p \sim 5 \times 10^{18}$ cm$^{-3}$) $E_F$ lies approximately 1.0 eV below the conduction band (i.e. $E_F = E_{cb} - 1.0$ eV) and approxi-

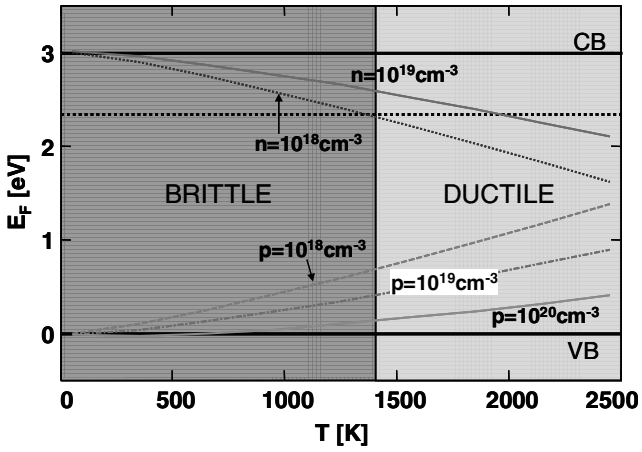


**Figure 1.8** Calculated variation of the Fermi energy with temperature. Typical growth temperatures are about 2100–2300 °C. The ductile to brittle transition temperature is the vertical line at a temperature of about 1400 K.

mately 1.0 eV above the valence band (i.e. $E_F = E_{vb} + 1.0$ eV) at $T = 2200$ °C. At the ductile to brittle transition temperature (1150 °C) [50], for the same doping concentrations, the calculated Fermi energies are approximately 0.5 eV below the conduction band for the n-type 6H-SiC : N and approximately 1.0 eV above the valence band for the p-type doped 6H-SiC : Al,B. At growth temperatures a BPD related defect level would need to lie near the band gap center for an electronic model leading to its suppression or favoring of its stability to be applicable.

No one has ever found or reported about threading edge and screw dislocations related energy levels. Glide and propagation of these dislocation types is not associated with stacking fault defects in the basal plane of hexagonal SiC, which are equivalent to a polytype transformation in a low dimension as is the case with glide of basal plane dislocations.

#### 1.3.1.2 **Cathodoluminescence measurements**

Cathodoluminescence measurements on p-type and n-type doped 6H-SiC indicate the presence of luminescence peaks in the visible and ultraviolet range as shown in Fig. 1.9. The peak corresponding to the energy level at 2.95 eV which is approximately the band gap of 6H-SiC is associated with band-to-band transitions. Those corresponding at 2.66 eV and 2.52 eV correspond to donor acceptor pair recombination (DAP). Apart from these two peaks both n-type and p-type 6H-SiC exhibit broad peaks in the red spectral range. However, the two transitions of approximately 1.8 eV and 1.9 eV, which are present in the n-type 6H-SiC are absent in the p-type 6H-SiC. These transitions

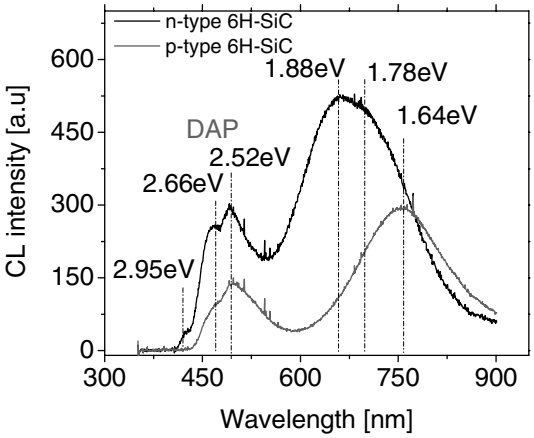


**Figure 1.9** Cathodoluminescence spectra of n-type and p-type doped SiC. Note the broad luminescence peaks in the red spectral range. The two peaks at about 1.9 eV and 1.8 eV present in this range in n-type doped 6H-SiC crystals, which are associated with basal plane dislocation, are absent in p-type doped crystals.

are related to basal plane dislocations, also previously reported by Ottaviani et al. [51] and Galeckas et al. [52] and would be compatible with electronic levels of about 1 eV below the conduction band minimum for n-type 6H-SiC or about 1 eV above the valence band maximum in the case of p-type 6H-SiC. In n-type doped 6H-SiC, at the ductile to brittle transition ($E_F \approx 0.5$ eV below the conduction band), the basal plane dislocation defect level is located near the donor level (but below the Fermi level). In this position, electron capture is more efficient than would be in p-type doped material with low electron concentration and where the defect level is above the Fermi level.

### 1.3.2
### Influence of growth temperature on dislocation evolution

Apart from doping, we have also observed that the temperature of crystal growth influences the overall dislocation density tremendously during PVT growth of SiC. In Fig. 1.10 dislocation statistics of two crystals, grown with different seed temperatures, are shown to depict the influence of the latter on dislocation density. Both crystals are nominally undoped n-type 6H-SiC and the growth temperatures differ by about 100 °C. All the crystals for the study of the effect of growth temperature on dislocation evolution were grown on the (0001)Si face. The dislocation density in the crystal with a lower seed temperature is about twice as high as the one with a higher seed temperature. This suggests that a lower dislocation density in SiC crystals can be achieved by high temperature growth.

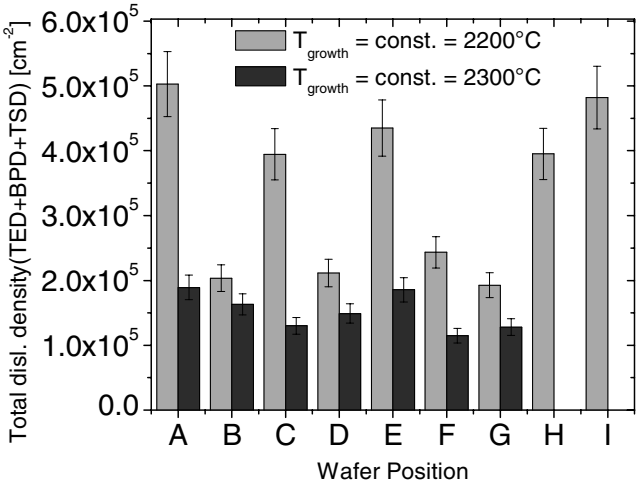


**Figure 1.10** Total dislocation densities of two nominally undoped n-type ($n \sim 10^{17}$ cm$^{-3}$) crystals grown at different temperatures (2200 °C and 2300 °C). Note the high total dislocation density in the crystal grown at the lower temperature.

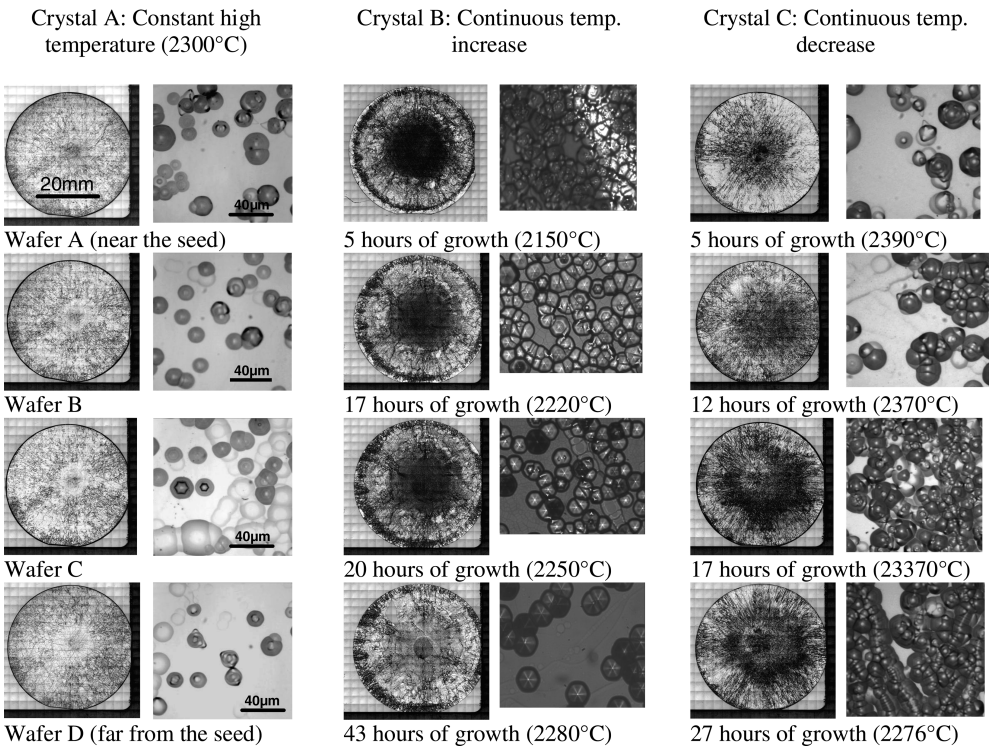


**Figure 1.11** Etching images of wafers of nominally undoped n-type ($n \approx 2 \times 10^{17}$ cm$^{-3}$) 6H-SiC crystals grown with different temperatures: constant high temperature of 2300 °C (crystal A), continuous temperature decrease (crystal B) and continuous temperature decrease (crystal C), showing the local variation of the dislocation density along the crystal growth axis. The images on the left of each column are dislocation mapping images obtained by low magnification optical microscopy.

A systematic investigation of the relationship between growth temperature and dislocation density was achieved by continuously changing (increasing/decreasing) the crystal growth temperature during growth. The temperature profiles for these growths are shown in Fig. 1.2. Figure 1.11 shows typical KOH etching images of crystals grown with continuous temperature increase, continuous temperature decrease and, for comparison, of a crystal grown with a high constant temperature (2300 °C). On the left of each column dislocation mapping over the whole wafer surfaces is shown. Here, the images were acquired at a lower magnification than those on the right. The darker regions in the mapping images correspond to a high dislocation density. Figure 1.12 summarizes the dislocation statistics in these crystals in relation to the crystal growth temperature.

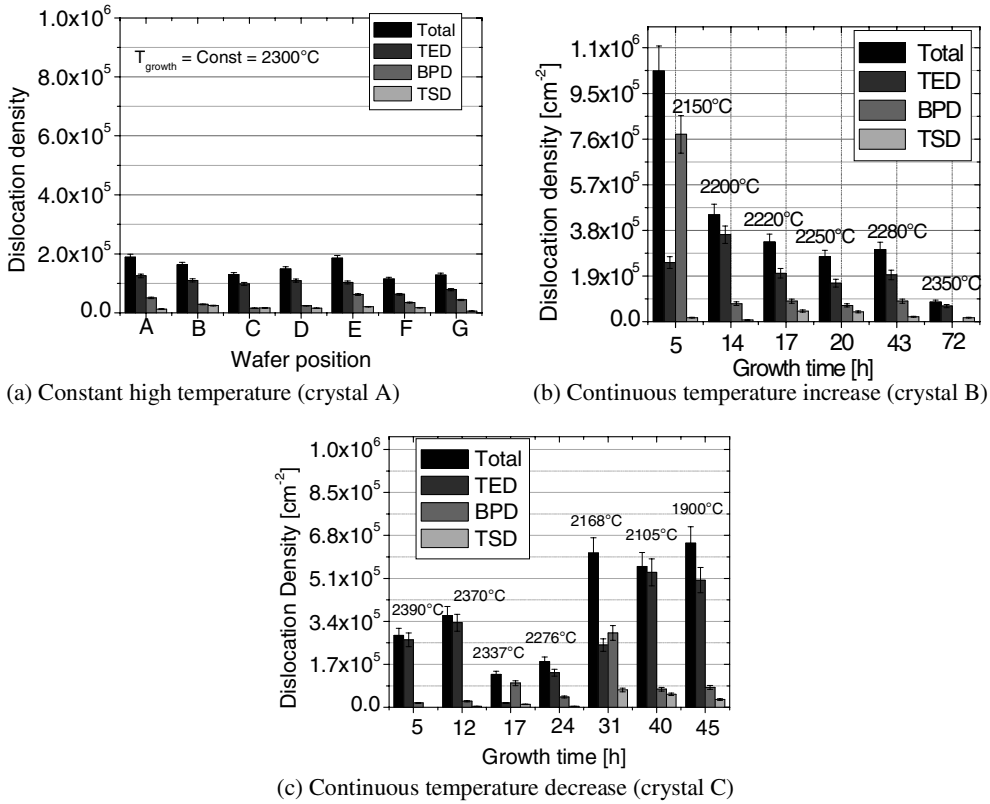


(a) Constant high temperature (crystal A)

(b) Continuous temperature increase (crystal B)

(c) Continuous temperature decrease (crystal C)

**Figure 1.12** Summary of the dislocation analysis over large wafer areas in crystals A, B, and C showing the statistics of threading edge dislocations, basal plane dislocations, and threading edge dislocations and their variation with the growth temperature.

The dislocation density in the crystals shows a sharp response to the temperature of crystal growth as depicted in Figs. 1.11 (images) and 1.12 (dislocation statistics). In crystal A, grown with a constant high temperature of about 2300 °C, we have observed a constant low dislocation density of about $2 \times 10^5$ cm$^{-2}$ along the crystal axis. This trend changes conspicuously in crystals grown with continuously changing growth temperature. In crystal B, grown with continuous temperature increase, the dislocation density decreases dramatically in the direction of increasing growth temperature, i.e. it is high at early growth stages (close to $10^6$ cm$^{-2}$), in low-temperature growth regimes, and then decreases abruptly with increasing temperature to a value of about $8 \times 10^4$ cm$^{-2}$. The seed used for this growth was characterized by KOH etching/optical microscopy and its average dislocation density was found to be about $1.2 \times 10^5$ cm$^{-2}$. The density in the middle of the seed, excluding the edge, was about $6.8 \times 10^4$ cm$^{-2}$. We attribute the high dislocation density at the initial

point of growth to low growth temperature because we did not observe such a high density in, e.g., crystal A in which the temperature was high in the early growth stages. In crystal C, grown with continuous temperature decrease, the trend in the dislocation density follows the reverse of that of crystal B, i.e. low dislocation density at early growth stages (high growth temperature regime) and high dislocation density at later stages (low growth temperature regime). Generally, the total dislocation density in the high-temperature growth regimes of crystals B and C, grown with a continuous change of the process temperature is comparable to that in crystal A, grown with a constant high temperature.

#### 1.3.2.1 **Rocking curves**

In Fig. 1.13 rocking curves of crystals grown at different temperature regimes are shown. The growth temperature of each crystal is indicated. The measurements were carried out using HE-XRD. In order to sidestep the influ-

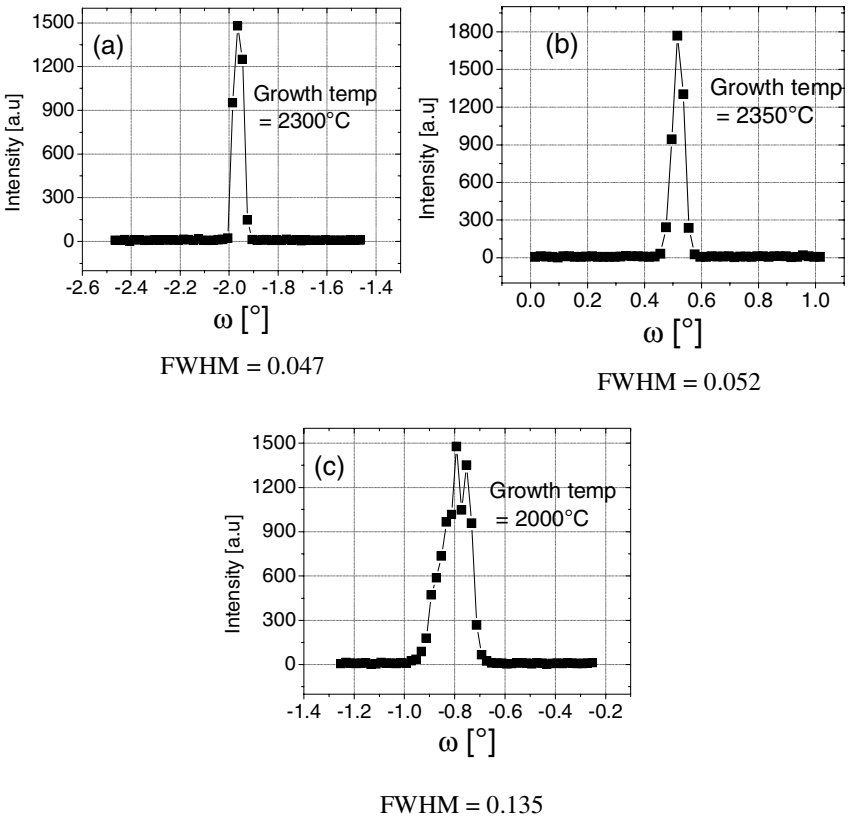


**Figure 1.13** (0006) rocking curves of portions of crystals A, B, and C grown in the indicated temperature regimes. Note the high value of the FWHM for low temperature growth.

ence of the polycrystalline rim and to obtain more comparable results, the HE-XRD measurements were confined to the facetted region of the crystals; the $(\bar{2}110)$ reflection was measured. The high-temperature-grown crystals exhibit narrow rocking curves (Fig. 1.13a and b) as compared to the low-temperature-grown counterpart (Fig. 1.13c). The FWHM is by a factor of about 3 greater in the low temperature grown crystal than the high temperature grown ones. This implies that in the low temperature grown sample a high mosaicity and many subgrain boundaries are present, which correlate with a high dislocation density as compared to those grown at high temperatures. This is in good agreement with the results of defect selective-etching (Fig. 1.11) and dislocation statistics (Fig. 1.12).

#### 1.3.2.2 **Lattice plane bending versus crystal growth temperature**

The study of lattice plane bending in relation to the temperature of crystal growth may provide additional information, which could lead to the improvement of the quality of PVT-grown SiC crystals in a general case. The measurements were carried out on the caps of crystals A, B and C; the $(\bar{2}110)$ reflection was measured. Figure 1.14 illustrates the measurement positions on a crystal cap. The temperatures at the phase boundaries of these crystals at the end of growth were 2300 °C, 2350 °C and 1900 °C, respectively. The crystals were positioned in the same crystallographic orientations during measurements. In Fig. 1.15 the results of lattice plane bending in the test samples are shown. The change in the peak positions of the rocking curves (lattice plane bending) at different positions across the crystal is indicated by the contrast of the square boxes in the figure from the middle of the facet to the outermost positions of the crystal. The value (in degrees) of the lattice plane bending is the change in contrast (indicating change in rocking curve peak position) from one end of the crystal to the other, and can be read off from the scale on the right hand side of the figure (the values for each position are indicated beside the boxes).

No lattice plane bending is observable in the sample taken from the crystal grown at constant high temperature (crystal A). The crystal, grown with continuous temperature increase (crystal B) shows the highest bending of lattice planes with a value of about 2°. The radius of curvature has been calculated to

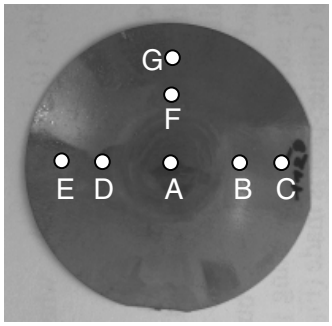


**Figure 1.14** Photograph of a cap of a 6H-SiC crystal to illustrate the measured positions during high energy X-ray diffraction measurements of the $(\bar{2}110)$ reflection for determining the lattice plane bending presented in Fig. 15.

be 0.9 m. The crystal, grown with continuous temperature decrease (crystal C) shows only a slight bending of about 0.3°; the calculated radius of curvature amounts to 2.9 m. These results demonstrate, clearly, a distinct relationship between lattice plane bending and the temperature of crystal growth. However, if sample A (crystal cap grown with constant high temperature) should exhibit low lattice plane bending, this would well be expected of sample B (from the crystal grown with continuous temperature increase). The crystal portions containing the caps in these two crystals were grown at high temperatures. Instead, sample C showed lesser lattice plane bending. This may be interpreted as follows: in the low-temperature growth regimes, crystal B must have acquired high lattice plane bending in such a way that even in the high-temperature growth regimes from which the test sample has been prepared the value remained high (up to 2°) and reduced bending could not be achieved. For crystal C, on the other hand, lattice plane bending at the early growth stages might have been equal to zero as is the case with crystal A because of the high temperatures. The low value of just 0.3° in this sample region, produced in low-tempe-rature growth regime, is an indication that the bending of the planes was still at its infancy and it may have probably intensified significantly if growth had to continue further at these low growth temperatures.

In the literature bending of lattice planes has been attributed to a temperature gradient during the growth process [53]. In this work, however, we did not alter the temperature gradients during the growth process. Furthermore, the age and properties of the graphite components used in the growth setups were the same. As such, no differences in the radial temperature gradient induced by the setup components could have existed. This leads us to believe that the observed lattice plane bending is due, fundamentally, to the differences in crystal growth temperature coupled with the related kinetic processes at the growth

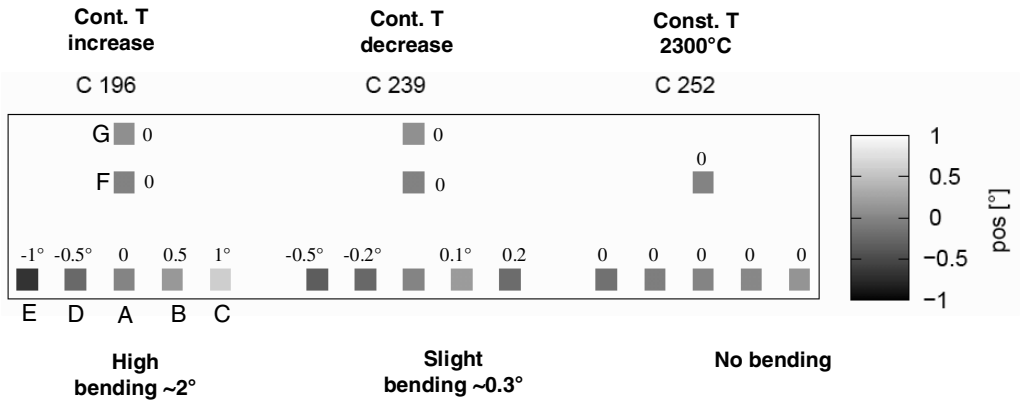


**Figure 1.15** Results of lattice planes bending in 6H-SiC crystals grown with different growth temperature profiles. Only the $(\bar{2}110)$ reflections of the final crystal parts containing the growth interfaces were measured.

interface (see Section 1.3.2.3). Evidently, the higher the process temperature during crystal growth, the lower the lattice plane bending.

Lattice plane bending may, on its own, induce the formation of dislocations, especially BPDs, due to the ensuing misorientation. Therefore, suppressing lattice plane bending may also mean reducing the dislocation density in the crystals.

#### 1.3.2.3 **Surface kinetics model for dislocation evolution**

Generally, a decreasing dislocation density from the seed region to the top of the crystal is observed during bulk growth of SiC (see e.g. Wang et al. [54]) and it is usually proposed that the dislocation density could be reduced by increasing the length of the crystals. However, the decrease in the dislocation density as observed by Wang et al. is very slight as compared to that observed in this work in the case of, e.g., growth by continuously increasing the growth temperature during growth.

One mechanism that may influence the reduction of the dislocation density along the crystal growth axis (e.g. crystal B) with increase in growth temperature may be annihilation of the dislocations. In this case dislocations with Burgers vector of the opposite sign may annihilate, depending on their proximity, and the annihilation rate may increase with increasing temperature. In particular, BPD annihilation may proceed even more rapidly due to their high mobility as a result of low activation energy for motion [55]. However, considering the increase in the dislocation density in crystal C as the growth temperature decreases, it becomes clear that high growth temperature does not only cause annihilation but its major impact on dislocations is the prevention of their formation through its influence on the kinetic processes on the growth interface.

Generally, during PVT growth of SiC, the powder sublimes into SiC molecular species in the gas phase, e.g., SiC, $Si_2C$, $SiC_2$ etc. [56]. The species are adsorbed on the SiC seed crystal surface, which is kept at a lower temperature with respect to the powder. To be incorporated into the crystal, the adsorbent has to migrate along the surface to a step (provided by a screw dislocation), and then to a kink, where it is finally incorporated into the crystal; the kink offers the best possibility energetically for the absorbent to be incorporated into the crystal rather than detached from the growth interface and driven back into the gas phase under the influence of the high growth temperature.

The surface mobility of the SiC molecular species on the growth front may affect dislocation formation tremendously, and it depends strongly on the temperature of crystal growth, i.e. the higher the temperature the more kinetic energy they will possess and, hence, the more probable they will reach the kinks. Thus, step flow growth mode is favored and the SiC crystal grows by a layer-by-layer addition of the SiC gas phase species. At low temperatures, however, the adsorbents are less mobile and nucleate freely and randomly on the growth surface, hence, forming many growth sites or islands. This may occur, most probably, when the adsorbed SiC molecular species are less mobile, particularly in the case of low temperature growth, and are unable to reach the kinks

because of lack of required energy. If a sufficient number of species are close together or coalesce a stable growth center may arise because some species will be adequately bonded together and, so, will not be driven back into the gas phase. Hence, the random formation of growth centers may be assumed to depend, like the dislocation density, inversely on the temperature of crystal growth. The interaction of the spirals from different growth sites may lead to enormous strain build-up in the crystal and, depending on the nature of the interaction, to the formation of dislocations (TSDs, TEDs and BPDs). Ma et al. suggest that the coalescence of the growth spirals can either be perfect or mismatched, the latter being the cause of screw dislocations [57]. However, while mismatched coalescence may particularly cause screw dislocations, coalescence in general may lead to strain in the crystal and, hence, to basal plane and threading edge dislocations. Therefore, if the density of free nucleation sites or growth islands is high, as it would occur during low temperature growth, a high dislocation density in the crystal would be expected. In high temperature crystal growth processes, where the mobility of the SiC molecular species is high because of their high kinetic energy, the formation of nucleation sites would be highly suppressed and a step flow growth mode will be predominant. Consequently, the surface area of the crystal, such as the facet in which such a regular step structure prevails and, also, the step width would be proportional to the applied temperature of crystal growth. This is because an increasing surface mobility of the SiC ad-molecules would also lead to a high step velocity. This line of argument has been supported by AFM investigations of the step structure of the growth fronts of the crystals and, also, by the diameters of the facets for the different growth temperatures as will be shown below. Both quantities provide, to a great extent, quantitative information about the surface mobility of the SiC molecular species at the growth interface for a given growth temperature.

#### 1.3.2.4 **AFM measurements**

Figure 1.16 shows the results of the AFM measurements in the facetted regions of the growth interfaces (caps) of the crystals grown with constant high temperature (crystal A, Fig. 1.16a), continuous temperature increase (crystal B, Fig. 1.16b), continuous temperature decrease (crystal C, Fig. 1.16c) and, in addition, of a crystal grown with constant but low temperature (crystal D, Fig. 1.16d). Photographs of the caps of the different crystals are included, showing the facets and their diameters. The temperatures of the growth interfaces at the end of the growth processes are given. The white arrows in Fig. 1.16a and b indicate the dimensions of the widths of the terraces. The white dots in Fig. 1.16d are particles that adhered to the surface of the crystal during the cooling process [58].

Crystals A, B, and D exhibit regular step structures and it is clear that there is a distinct relationship between the terrace width and the temperature of the growth front (growth temperature of the crystal). The regular step structure for temperatures above 2100 °C is an indication of a layer-by-layer growth, char-

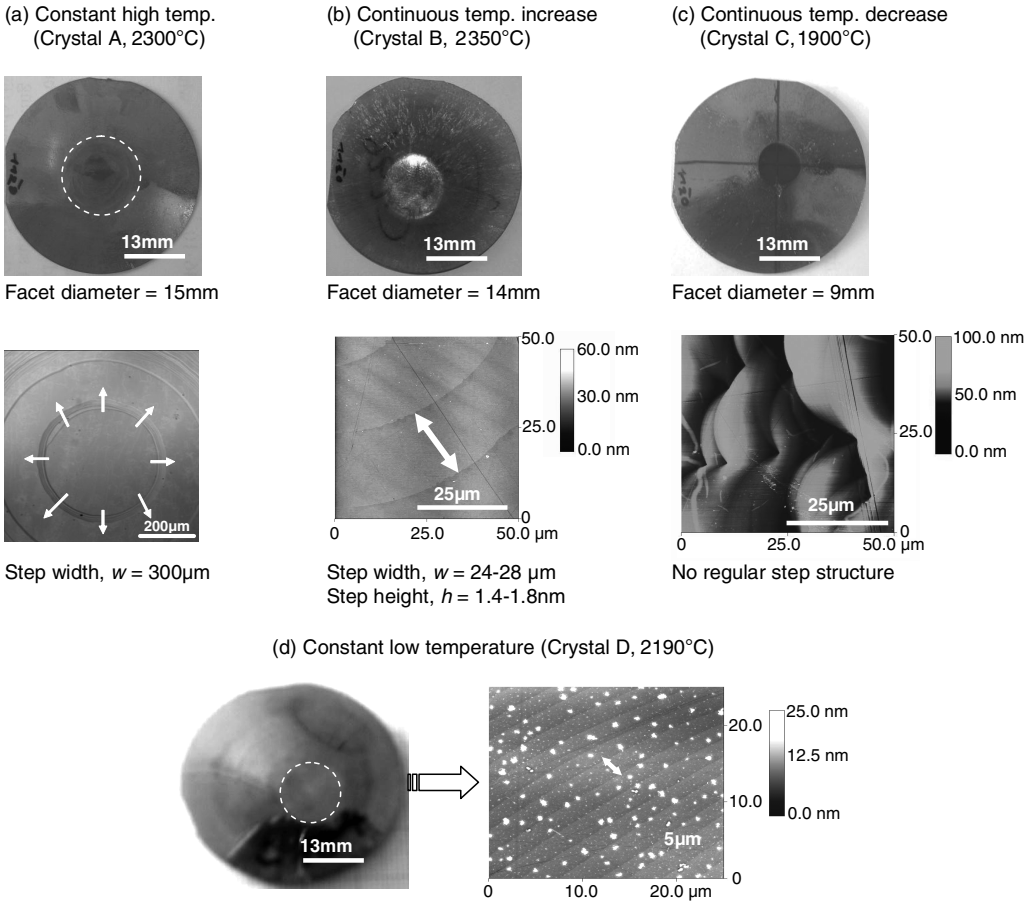


**Figure 1.16** AFM images showing the step structure in the center of the facets of the growth interfaces of the crystals grown with different temperature profiles (crystals A, B, C, and D) and photographs of their caps.

acterized by a regular step flow, whereby the terrace width is indicative of the step flow velocity. In crystal D, with a relatively lower growth or interface temperature, macrosteps with terrace widths $w$ ranging from 2–3 µm are observed (Fig. 1.16d) with a height, $h$, in the range 1.4–1.7 nm, which is about the lattice parameter $c$ for 6H-SiC [58]. In crystal A (Fig. 1.16a) and B (Fig. 1.16b) with higher growth front temperatures wider terraces are observed. In crystal B $w$ ranges from 24–28 µm and $h$ is in the range 1.4–1.8 nm. In crystal A with approximately the same growth front temperature (but constant during the entire growth period) $w$ is so large that the step structure could not be determined by AFM measurements because the terrace widths of the steps were out of the measurement range of the apparatus. The step structure in

this crystal was observed by optical microscopy. The terrace width was over 100 μm and in the center of the facet a perfectly circular and planar ring with a diameter of about 600 μm, without a spiral was observed (Fig. 1.16a). From the step configuration and width of their terraces it is clear that the growth was dominated by step flow mechanism with a very high step velocity or lateral growth rate indicated by the arrows in Fig. 1.16a. Also, it can be suggested that little or no lattice plane bending would occur in such a growth mode because of the layer-by-layer addition of SiC building blocks. This is in conformity with the observations of HE-XRD investigations. The difference in $w$ between crystals A and B may be due to the fact that in A high temperature growth started from the beginning and continued till the end of growth, whereas in B one may assume that the step structure continued to be modified as the temperature of the growth front increased progressively, i.e. from small step widths in the low-temperature growth regimes to large ones in high-temperature growth ones. Crystal C shows no regular step structure. The distorted step structure with wide ridges or hillocks (Fig. 1.16c) suggests a preceding step structure in the initial high-temperature growth regime that is regular and with wide terraces, similar to crystal A and B. However, with a reduction in growth temperature free nucleation and, hence, island formation in the large terraces probably distorted the step structure because of step flow misorientation.

Also, the diameters of the facets provide additional quantitative information about the surface mobility of the SiC gas phase species of the 6H-SiC crystals. The diameter has been observed to be proportional to the temperature of crystal growth. A large facet diameter, like the terrace width, signifies a high step flow velocity (high lateral growth). Crystals with large facets have also been observed to exhibit wide terraces and low dislocation densities. Crystals A and B (B in the high temperature growth regime) exhibit large facets with diameters of 15 mm and 14 mm, respectively. That of crystal C is quite small (9 mm). In another crystal, also grown with continuous temperature decrease (crystal E), we observed a facet composed of an inner and an outer facet as shown in the photograph in Fig. 1.17. The outer facet, $F_1$, with a larger diameter of about 20 mm is the facet in the high-temperature growth regime and

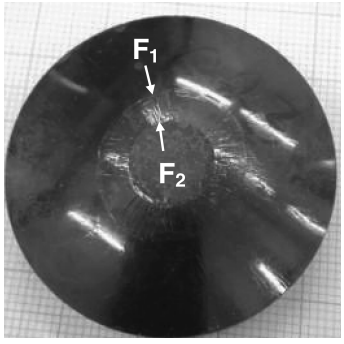


**Figure 1.17** Photograph of a crystal cap grown with continuous temperature decrease (crystal E) showing facet shrinkage with decreasing growth temperature.

the inner facet, $F_2$, with a diameter = 10 mm, the facet in low-temperature growth regime. Thus, by de-creasing the temperature continuously by about 350 °C over the growth period, facet diameter shrinkage of about 50% occurred. This value reflects, approximately, the percentage by which the surface mobility of the SiC molecular species must have been reduced as a result of the reduced growth temperature.

#### 3.3.2.5 Estimation of the surface mobility from the terrace width

The surface mobility, $v_{x,}$ is the speed of a SiC gas phase species from the point it is adsorbed on the growth surface until it reaches a kink, where it is finally incorporated into the crystal. Assuming that the species lands in the middle of a terrace of width $w$, the distance it covers to reach the kink, $\Delta x,$ is equal to half of the terrace width, i.e. $1/2w$ assuming that it makes a straight path to the kink. The time, $\Delta t$, to cover this distance is approximately equal to the time to grow a unit step height, $h$ = 1.6 nm (for 6H-SiC). This time can be estimated from the growth rate of the crystal. Thus, the surface mobility is

$$v_x = \frac{\Delta x}{\Delta t} = \frac{w}{2\Delta t}. \quad (1)$$

In the case of constant high temperature growth of 2300 °C (crystal A), for instance (growth rate 220 µm/h), $\Delta t$ is about 0.03 s. The step width of this crystal at the center of the facet is $w$ = 300 µm. The surface mobility is, therefore, 5000 µm $s^{-1}$.

Table 1.2 summarizes the surface mobilities with respect to growth temperature for the investigated crystals. It should be noted that for the crystal grown with continuous temperature increase (crystal B) the growth rate was not constant throughout the growth process. Using the *in-situ* X-ray imaging technique we were nevertheless able to determine the rate for the portion of the crystal in the high-temperature growth regime, where the measurements have been conducted. The error in the measurement of the growth rate, *in-situ* during growth was about 10%. The surface mobility of crystal C could not be determined because the step width could not be measured. The high growth rate of crystal D was due to the low process pressure for this growth. Generally, the value of the surface mobility increases with the growth temperature and is highest for the crystal that was grown at high constant temperature (crystal A).

**Table 1.2** Temperature dependent surface mobility of SiC molecular species on the growth interface during the PVT growth process of bulk 6H-SiC.

| crystal | temperature of growth interface (°C) | growth rate of crystal/ region with cap (µm/h) | step terrace, $w$ (µm) | time, $\Delta t$, to grow a unit step height (s) | surface mobility (µm/s) |
|---|---|---|---|---|---|
| A | 2300 | 220 | 300 | 0.03 | 5000 |
| B | 2350 | 200 | 28 | 0.03 | 486 |
| D | 2190 | 300 | 3 | 0.02 | 78 |

The value is, off course, lower in crystal B because of the smaller terrace widths than in crystal A.

## 1.4 Spatial distribution of dislocations in SiC

We have observed a characteristic alignment of dislocations in 4H-SiC and 6H-SiC on the vicinal (0001)Si surfaces in the form of linear arrays and also in cell structures.

Figure 1.18 shows optical and SEM micrographs of etch pits in 6H-SiC crystals that depict the dislocation alignment in linear arrays. Figure 1.18b is a high magnification image of the area indicated in Fig. 1.18a. Dislocation distribution over the wafer surface occurs in three main ways, independent of the doping type or polytype, i.e. 6H-SiC or 4H-SiC: (i) the dislocations are aligned in linear arrays (low angle grain boundaries), (ii) they are arranged in cell structures, and (iii) they occur as single spots on the surface of the wafer.

In the configuration in linear arrays, the arrays are parallel to each other and are aligned in the $(1\bar{1}00)$ direction and in a direction making an angle of about 45°–60° to the latter (Fig. 1.18b–d). From the SEM, the dislocations in the arrays are predominantly those of edge character (Fig. 1.18e). Those of screw

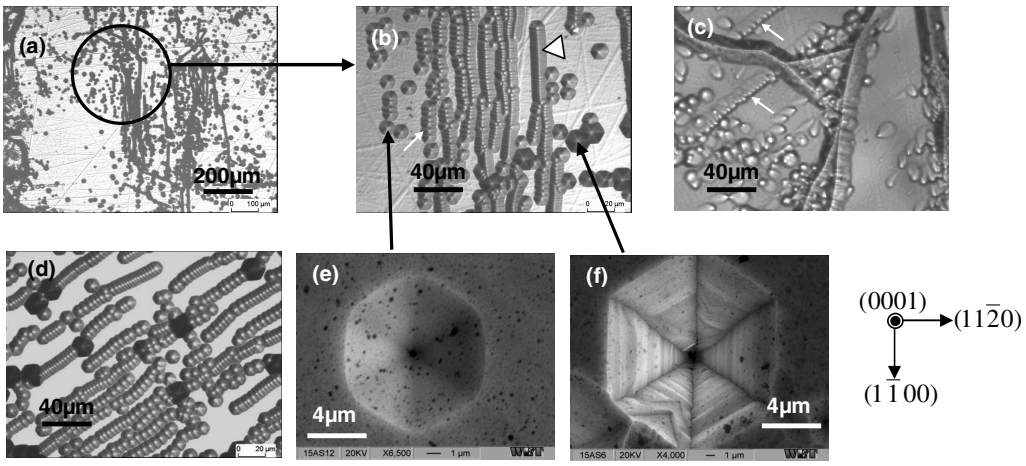


**Figure 1.18** Low magnification optical micrograph (a), high magnification optical micrographs (b)–(d), and SEM micrographs (e and f) of etch pit arrays of dislocations in 6H-SiC. (a), (b), and (d) are images of a p-type doped crystal, while (c) is an image from an n-type doped crystal. Both single arrays of threading edge (b) and (d) and basal plane (c) dislocations and wide band arrays are shown. SEM reveals that the dislocations in the arrays are predominantly those with an edge character.

character, like the ones shown in Fig. 1.18f, are hardly observed in such long linear configurations. However, short arrays of 3–5 dislocations occur. BPDs also show alignment in long linear arrays as can be seen in Fig. 1.18c (image from an n-type doped 6H-SiC). These are indicated by the white arrows in the figure. The dislocation density in the arrays is particularly high, reaching a value of about $2 \times 10^6$ cm$^{-2}$; the linear dislocation density ranges from $5 \times 10^2$ cm$^{-1}$ to $6 \times 10^3$ cm$^{-1}$ (compare e.g. the array marked by the white triangle and the one marked by the white arrow in Fig. 1.18b). The same variation is observed in the case in which the linear arrays are composed of BPDs (Fig. 1.18c). Striking, in the configuration of the dislocations, is their alignment in linear arrays in specific crystallographic directions, i.e. in the $(1\bar{1}00)$ direction (Fig. 1.18b) and about 45°–60° to this (Fig. 1.18c and d). In the etching images of whole wafer dislocation mapping in Fig. 1.11 a six-fold symmetry of dislocation alignment can clearly be observed, especially in crystal B. Here, also, the alignment does follow the crystallographic direction $[1\bar{1}00]$ and at angles of about 45°– 60° relative to this direction and their equivalents.

Ha et al. made similar observations in PVT grown SiC using KOH etching [59, 60]. They showed by TEM that the dislocations in the arrays are pure edge dislocations and also, that some arrays are composed entirely of BPDs [60]. They hold that the TED pile-ups are a result of polygonization (reduction of the strain in the crystal through overlap of the strain fields of individual dislocations), while the BPD arrays result from slip traces of high temperature deformation during the growth process.

Besides forming linear arrays, we have also observed that the dislocations in SiC usually arrange themselves in cell structures. Figure 1.19 shows selected images showing dislocation cell structures in SiC, i.e. n-type 6H-SiC wafer (Fig. 1.19a) and p-type 6H-SiC wafer (Fig. 1.19b–c). Comparable to the alignment in linear arrays, the dislocation density is very low inside the cell but high at the cell boundaries, which are actually low angle grain boundaries. Usually, in cases, where the cell boundaries are marked by linear arrays, the ar-

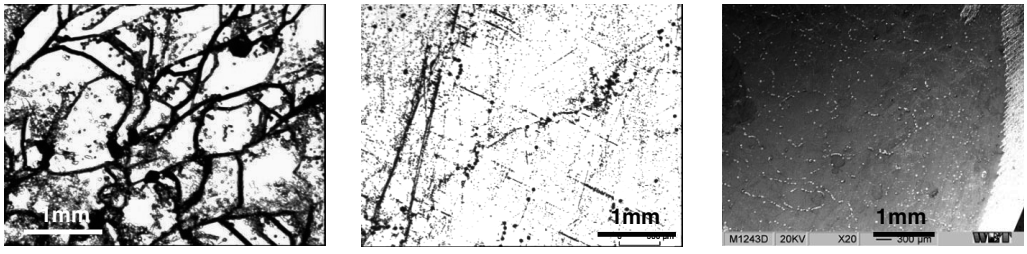


(a) (b) (c)

**Figure 1.19** KOH etching images on the (0001)Si face of 6H-SiC wafers taken by low magnification optical microscopy (a)–(b) and SEM (c) showing the patterning of the dislocations in cellular structures. (a) is an n-type doped 6H-SiC wafer and (b) and (c) are p-type doped ones.

rays tend to align themselves in the [1 $\bar{1}$00] direction and at angles of about 45°–60° relative to this direction. The cellular nature of dislocations can best be observed by low magnification microscopy (optical or SEM). As in the case of alignment in linear arrays, no substantial distinction of the cell structures in p-type and n-type doped SiC is observable.

Patterning of dislocations into cells has been observed by other research groups in other compound semiconductors, e.g., GaAs, PbTe, CdTe and, also, in metals and metallic alloys [61–63]. One mechanism for their formation may be energy related, i.e. the reduction of the strain energy by clustering of the dislocations at the cell and grain boundaries, whereby the overlapping strain energies of individual dislocations reduces the overall strain energy in the crystal, similar to the case of dislocation arrays. However, according to Rudolph [61], the patterning may also be driven by self-organizing processes in the framework of equilibrium or non-equilibrium thermodynamics, where the rate of entropy produced within the crystal at high temperatures evokes self-ordered patterning of the already present or currently generated dislocations.

## 1.5 Conclusions

The evolution and dynamic properties of dislocations in SiC bulk crystals, grown by the physical vapor transport (PVT) method have been studied with respect of the process parameters doping and growth temperature. A statistical approach has been implemented for dislocation analysis after defect selective etching of the wafers in molten KOH. High energy X-ray diffraction (HE-XRD) and atomic force microscopy (AFM) measurements have been performed to further analyze the material. The full width at half maximum (FWHM) of the rocking curves and bending of lattice planes from HE-XRD measurements, and, also, the step structure of the growth front from AFM measurements have been correlated to the dislocation densities in the crystals as determined by defect selective etching.

It is shown that there is a doping type preference in the way stress relaxation occurs in *c*-plane-grown 6H-SiC single crystals. n-type doped 6H-SiC demonstrates a high ratio of basal plane dislocation (BPD) density to the total dislocation density, suggesting that stress relaxation takes place favoring entirely the generation of the latter dislocation type. In p-type doped 6H-SiC, on the other hand, the low ratio of BPDs to the total dislocation density or their absence in the material indicates that in this doping type stress relaxation takes place, favoring mostly the generation of threading edge and threading screw dislocations. By considering the position of the Fermi level and supporting cathodoluminescence (CL) measurements in both n-type and p-type doped materials it is shown that the electronic nature of p-type doped SiC tends to suppress the generation or propagation of BPDs in the material. If BPD generation or propagation in SiC can be lowered or even suppressed completely by p-type

doping this could have a tremendous impact on the stacking fault problem in SiC power devices because their operation-induced generation and expansion will be suppressed as well.

The temperature of crystal growth is shown to have a great impact on the evolution of dislocations and their density in 6H-SiC crystals; high growth temperatures lead to a low dislocation density, while low growth temperatures lead to a high dislocation density. The bending of lattice planes also shows a similar trend, i.e. low bending for high-temperature crystal growth and high bending for low-temperature growth. Noteworthy is also the low ratio of basal plane dislocation density in high temperature grown crystals over low temperature grown ones. It could be shown that the overall dislocation density in the crystals, likewise the bending of lattice planes are limited by kinetic effects during the growth process, i.e. the surface mobility of the gas phase species on the SiC growth interface and, hence, determine, to a large extend, the crystal quality. High growth temperatures favor a high surface mobility, leading to a high step flow velocity and, hence, flat lattice planes. Lattice plane bending appears to be greatly limited by kinetic effects during crystal growth (surface mobility). Since the bending of lattice planes and the interaction of growth spirals that are associated with dislocation formation in 6H-SiC crystals can be suppressed by high temperature growth, it is evident that the latter is an important technological aspect for the growth of high quality SiC crystals.

Generally, the positive impact of p-type doping and high crystal growth temperature on the quality of 6H-SiC bulk crystals could be demonstrated.

## Acknowledgements

This work was funded by the Deutsche Forschungsgemeinschaft (DFG) under contract number WE2107/3 in the frame of the Forschergruppe FOR476.

## References

1. T. L. Straubinger, M. Bickermann, R. Weingärtner, P. J. Wellmann, and A. Winnacker, J. Cryst. Growth **240**, 117–123 (2002).
2. P. Wellmann, P. Desperrier, R. Mueller, T. Straubinger, A. Winnacker, F. Baillet, E. Blanquet, J. M. Dedulle, and M. Pons, J. Cryst. Growth **275** (1–2), e555–e560 (2005).
3. P. Wellmann, Compd. Semicond. (March), 23/24 (2005).
4. P. Wellmann, R. Müller, and M. Pons, Mater. Sci. Forum **527–529**, 75–78 (2006).
5. P. Wellmann, R. Müller, D. Queren, S. A. Sakwe, and M. Pons, accepted for publication in Surf. Coat. Technol. **201**(7), 4026–4031 (2006), icmctf2006 proceedings.
6. R. Müller, U. Künecke, R. Weingärtner, H. Schmitt, P. Desperrier, and P. Wellmann, Mater. Sci. Forum **483–485**, 31–34 (2005).
7. P. Desperrier, R. Müller, A. Winnacker, and P. J. Wellmann, Mater. Sci. Forum **457–460**, 727–730 (2004).
8. M. Wagner, E. Mustafa, S. Hahn, M. Syväjärvi, R. Yakimova, S. Jang,

S. A. Sakwe, and P. Wellmann, Mater. Sci. Forum **556/557**, 327–330 (2007).
**9.** R. Püsche, M. Hundhausen, L. Ley, K. Semmelroth, G. Pensl, P. Desperrier, P. J. Wellmann, E. E. Haller, J. W. Ager, and U. Starke, Mater. Sci. Forum **527–529**, 579–584 (2006).
**10.** R. Müller, U. Künecke, A. Thuaire, M. Mermoux, M. Pons, and P. Wellmann, phys. stat. sol.(c) **3**(3), 558–561 (2006).
**11.** S. Contreras, M. Zielinski, L. Konczewicz, C. Blanc, S. Juillaguet, R. Müller, U. Künecke, P. Wellmann, and J. Camassel, Mater. Sci. Forum **527–529**, 633–636 (2006).
**12.** P. Wellmann, T. Straubinger, R. Mueller, M. Pons, A. Thuaire, A. Crisci, M. Mermoux, and L. Auvray, Mater. Sci. Forum **483–485**, 393 (2005).
**13.** P. J. Wellmann, T. Straubinger, U. Künecke, R. Müller, S. A. Sakwe, M. Pons, A. Thuaire, A. Crisci, M. Mermoux, L. Auvray, and J. Camassel, phys. stat. sol. (a) **202**(4), 598–601 (2005).
**14.** H. Schmitt, R. Müller, M. Maier, A. Winnacker, and P. Wellmann, Mater. Sci. Forum **483–485**, 445 (2005).
**15.** R. Weingärtner, P. J. Wellmann, and A. Winnacker, Mater. Sci. Forum **457–460**, 645 (2004).
**16.** P. J. Wellmann and R. Weingärtner, Mater. Sci. Eng. B **102**, 262–268 (2003).
**17.** R. Weingärtner, A. Albrecht, P. J. Wellmann, and A. Winnacker, Mater. Sci. Forum **433–436**, 341 (2003).
**18.** R. Weingärtner, M. Bickermann, Z. Herro, U. Künecke, S. A. Sakwe, P. J. Wellmann, and A. Winnacker, Mater. Sci. Forum **433–436**, 333 (2003).
**19.** P. J. Wellmann and M. Pons, J. Cryst. Growth **303**, 337–341 (2007).
**20.** M. Pons, S. Nishizawa, P. Wellmann, M. Ucar, E. Blanquet, J. M. Dedulle, F. Baillet, D. Chaussende, C. Bernard, and R. Madar, Numerical simulation of SiC processes: A characterisation tool for the design of epitaxial structures in electronics, in: Proc. EUROCVD-15, Bochum, Germany, 4–9 September 2005, Electrochemical Society Proceedings.
**21.** M. Pons, E. Blanquet, F. Baillet, D. Chaussende, J. M. Dedulle, E. Pernot, R. Madar, P. Wellmann, and M. Ucar, Mater. Sci. Forum **483–485**, 3–8 (2005).
**22.** Z. G. Herro, P. J. Wellmann, R. Püsche, M. Hundhausen, L. Ley, M. Maier, P. Masri, and A. Winnacker, J. Cryst. Growth **258**(1–3), 261–267 (2003).
**23.** P. J. Wellmann, Z. Herro, S. A. Sakwe, P. Masri, M. Bogdanov, S. Karpov, A. Kulik, M. Ramm, and Y. Makarov, Mater. Sci. Forum **457–460**, 55–58 (2004).
**24.** Y.-S. Jang, S. A. Sakwe, P. J. Wellmann, S. Juillaguet, J. Camassel, and J. W. Steeds, Mater. Sci. Forum **556/557**, 13–16 (2007).
**25.** P. J. Wellmann, D. Queren, U. Künecke, R. Müller, S. A. Sakwe, A. Thuaire, M. Mermoux, M. Pons, and J. Camassel, Proceedings of the 8th German–Vietnamese Workshop on Physics and Engineering, Erlangen, 4–8 April 2005.
**26.** S. A. Sakwe, R. Müller, D. Queren, U. Künecke, and P. J. Wellmann, phys. stat. sol. (c) **3**(3), 567–570 (2006).
**27.** P. J. Wellmann, D. Queren, R. Müller, S. A. Sakwe, and U. Künecke, Mater. Sci. Forum, **527–529**, 79–82 (2006).
**28.** K. Konias, R. Hock, M. Stockmeier, P. Wellmann, and A. Magerl, Mater. Sci. Forum **556/557**, 267–270 (2007).
**29.** P. J. Wellmann, M. Bickermann, D. Hofmann, L. Kadinski, M. Selder, T. L. Straubinger, and A. Winnacker, J. Cryst. Growth **216**, 263 (2000).
**30.** P. J. Wellmann, T. L. Straubinger, P. Desperrier, R. Müller, U. Künecke, S. A. Sakwe, H. Schmitt, A. Winnacker, E. Blanquet, J.-M. Deulle, and M. Pons, Mater. Sci. Forum **483–485**, 25–30 (2005).
**31.** R. Weingärtner, P. J. Wellmann, M. Bickermann, D. Hofmann, T. L.

Straubinger, and A. Winnacker, Appl. Phys. Lett. **80**(1), 70–72 (2002).
**32.** R. Müller, U. Künecke, R. Weingärtner, M. Maier, and P. J. Wellmann, phys. stat. sol. (c) **3**(3), 554 (2006).
**33.** P. J. Wellmann, M. Bickermann, D. Hofmann, L. Kadisnki, M. Selder, T. L. Straubinger, and A. Winnacker, J. Cryst. Growth **216**, 263 (1999).
**34.** S. A. Sakwe, R. Müller, and P. J. Wellmann, J. Cryst. Growth **289**, 520–526 (2006).
**35.** C. Seitz, M. Weisser, M. Gomm, R. Hock, and A. Magerl, J. Appl. Crystallogr. **37**, 901–910 (2004).
**36.** S. Ha, W. M. Vetter, M. Dudley, and M. Skowronski, Mater. Sci. Forum **389–393**, 443 (2002).
**37.** J. L. Weyer, S. Lazar, J. Borysiuk, and J. Pernot, phys. stat. sol. (a) **202**, 578 (2005).
**38.** R. Chierchia, T. Böttcher, H. Heinke, S. Einfeldt, S. Figge, and D. Hommel, J. Appl. Phys. **93**(11), 8918 (2003).
**39.** R. W. Vook, X. H. Wu, S. Keller, Y. Li, D. Kapolnek, and B. P. Keller, Appl. Phys. Lett. **68**(5), 643 (1996).
**40.** P. Lukác and Z. Trojanová, Mater. Sci. Eng. A **462**, 23 (2007).
**41.** K. Sumino and I. Yonenaga, Solid State Phenom. **85/86**, 145 (2002).
**42.** A. K. Semennikov, S. Y. Karpov, and M. S. Ramm, Mater. Sci. Forum **457–460**, 383 (2004).
**43.** J.-M. Spaeth, Mater. Sci. Forum **338–342**, 785–790 (2000).
**44.** S. Greulich-Weber, M. Feege, J.-M. Spaeth, E. N. Kalabukhova, S. N. Lukin, and E. N. Mokhov, Solid State Commun. **93**(5), 393 (1995).
**45.** P. J. Wellmann, P. Hens, S. A. Sakwe, D. Queren, R. Müller, K. Durst, and M. Göken, Mater. Sci. Forum **556/557**, 259–262 (2007).
**46.** H. Itoh, A. Kawasuso, T. Ohshims, M. Yoshikawa, I. Nashiyama, S. Tanigawa, S. Misawa, H. Okumura, and S. Joshida, phys. stat. sol. (a) **162**, 173 (1997).
**47.** Hisaomi Iwata, Ulf Lindefelt, Sven Öberg, and P. R. Briddon, Microelectron. J. **34**, 371–374 (2003).
**48.** A. T. Blumenau, M. I. Heggie, C. J. Fall, R. Jones, and T. Frauenheim, Phys. Rev. B **65**, 205205 (2002).
**49.** P. Grivickas, V. Grivickas, A. Galeckas, and J. Linnros, Mater. Sci. Forum **389–393**, 617 (2002).
**50.** J. L. Demenet, M. H. Hong, and P. Pirouz, Mater. Sci. Forum **338–342**, 517 (2000).
**51.** L. Ottaviani, H. Idrissi, P. Hidalgo, M. Lancin, and B. Pichaud, phys. stat. sol. (c) **2**(6), 1792 (2005).
**52.** A. Galeckas, J. Linnros, and P. Pirouz, Appl. Phys. Lett. **81**(5), 883 (2002).
**53.** C. Seitz, Z. G. Herro, B. M. Epelbaum, R. Hock, and A. Magerl, J. Appl. Crystallogr. **39**, 17 (2006).
**54.** Shizhong Wang and Jibao He, Mater. Sci. Eng. B **83**, 8–12 (2001).
**55.** H. Idrissi, G. Regula, M. Lancin, J. Douin, and B. Pichaud, phys. stat. sol. (c) **2**(6), 1998 (2005).
**56.** A. Fissel, J. Cryst. Growth **212**, 438 (2000).
**57.** X. Ma, J. Appl. Phys. **99**, 063513 (2006).
**58.** N. Ohtani, M. Katsuno, A. Takahashi, T. Fujimoto, H. Tsuge, H. Yashiro, and M. Kanaya, J. Cryst. Growth **210**, 613 (2000).
**59.** Seoyong Ha, N. T. Nuhfer, G. S. Rohrer, M. De Graef, and M. Skowronski, J. Cryst. Growth **220**, 308–315 (2000).
**60.** Seoyong Ha, M. Skowronski, W. M. Vetter, and M. Dudley, J. Appl. Phys. **92**(2), 778–785 (2002).
**61.** P. Rudolph, Cryst. Res. Technol. **40**(1/2), 7–20 (2005).
**62.** P. Rudolph, C. Frank-Rotsch, U. Juda, M. Naumann, and M. Neubert, J. Cryst. Growth **265**, 331–340 (2004).
**63.** T. Tuomi, L. Knuutila, J. Riikonen, P. J. Mcnally, W.-M. Chen, J. Kanatharana, M. Neubert, and P. Rudolph, J. Cryst. Growth **237–239**, 350–355 (2002).